communications earth & environment

ARTICLE

https://doi.org/10.1038/s43247-021-00257-w OPEN

Micro-scale dissolution seams mobilise carbon in deep-sea limestones

Christoph E. Schrank[1✉], Michael M. W. Jones[2✉], Cameron M. Kewish[3], Grant A. van Riessen[4], Kathryn E. Elphick[1], Craig R. Sloss[1], Luke D. Nothdurft[1], Gregory E. Webb[5], David J. Paterson[3] & Klaus Regenauer-Lieb[6]

Measuring the amount of carbon captured in deep-sea limestones is fundamental to understanding the long-term carbon cycle because pelagic limestones represent Earth's largest carbon sink since the mid-Mesozoic. However, their contribution to the long-term carbon cycle is poorly quantified. Here, we use X-ray fluorescence and scanning X-ray diffraction microscopy for high-resolution chemical and structural analysis of pelagic limestone from the Paleocene Kaiwhata Formation in New Zealand. We identify densely packed diagenetic micro-dissolution seams that are invisible to light and electron-beam microscopes in most cases. Mass-balance calculations indicate that individual seams remove ~50% of the calcite mud matrix while their bulk-sample carbon loss adds up to ~10%. The liberated carbon is trapped in situ as calcite cement or returned to the ocean during physical compaction or soft-sediment deformation. We suggest micro-dissolution structures may play an important role in the long-term carbon cycle by modulating carbon exchange between the geosphere and hydrosphere.

[1] School of Earth and Atmospheric Sciences, Queensland University of Technology, Brisbane, QLD, Australia. [2] Queensland University of Technology, Central Analytical Research Facility, Brisbane, QLD, Australia. [3] Australian Synchrotron, Clayton, VIC, Australia. [4] La Trobe University, Chemistry and Physics, La Trobe Institute for Molecular Science, Melbourne, VIC, Australia. [5] School of Earth and Environmental Sciences, University of Queensland, St. Lucia, QLD, Australia. [6] School of Minerals and Energy Resources Engineering, The University of New South Wales, Kensington, NSW, Australia.
✉email: christoph.schrank@qut.edu.au; mw.jones@qut.edu.au

The long-term carbon cycle is largely driven by plate tectonics and operates on geological time scales of tens to hundreds of millions of years[1]. Quantitative models of the associated carbon budget have improved greatly through better estimates of carbon uptake in the oceanic lithosphere due to hydrothermal alteration, fluid-mediated carbon transfer in the mantle and lithosphere, and carbon venting due to volcanism or diffuse processes[1–5]. However, the large contribution of marine sediments to the long-term carbon cycle is not well understood. For example, the present-day carbon flux provided by deep-sea sediments is uncertain, with estimates ranging from 13[2] to 60[6] million tonnes of carbon per annum (Mt C/a) delivered to subduction zones. Even at the lower end of the range, pelagic sediments contribute substantially to the geological carbon budget and place deep-sea marine sediments as Earth's largest carbon sink[7,8]. Carbonate minerals sequester most of this carbon[9,10], typically in calcite[11] ($CaCO_3$). Therefore, mechanisms and rates of calcite accumulation and dissolution must be determined to develop quantitative carbon-budget models for deep-sea carbonates[10,11].

Here, we study diagenetic calcite dissolution in exhumed Paleocene deep-sea limestones from the Pahaoa river mouth, Wairarapa, New Zealand, to quantify how much carbon is mobilised by this mechanism. These limestones, attributed to the Kaiwhata Formation[12], formed in a deep ocean basin along New Zealand's passive margin before their entrainment into the accretionary wedge of the Hikurangi subduction zone ca. 25 million years ago[13,14] (see Supplementary Note 1 for geological background). Kaiwhata limestone outcrops around Pahaoa show abundant evidence for diagenetic calcite mobilisation through pressure dissolution accommodated by bedding-parallel stylolites (Fig. 1). Stylolites are localised dissolution surfaces with strong roughness that display a characteristic tooth-like or wave-like geometry[15,16] (Figs. 1 and 2). Their "teeth" contain important geological information. They point in the direction of the maximum principal stress σ_1 during pressure dissolution and thus record palaeo-stress orientation[17]. Peak morphology can be inverted for the magnitudes of the stress tensor components[18,19] while peak amplitudes provide a minimum estimate of the thickness of the dissolved rock layer[16]. However, stylolite peak amplitudes generally underestimate compaction[17] (Fig. 2a). Better estimates of volume change and material loss are obtained from strain markers[16,20], or ideally, mass-balance calculations underpinned by quantitative chemical data[21]. Stylolites contain a seam of insoluble residue that accumulates passively within the dissolution zone, including potential newly grown minerals[16] (Figs. 1b, 2). By measuring the concentrations of insoluble phases within the residue and the surrounding host rock, mass loss and gain can be computed[22,23] (see the "Methods" section). Previous bulk chemical analyses[24] of stylolite residue in limestones found that the oxides of Al, Fe, P, Si, and Ti are enriched by 5–20 times relative to host rock while CaO is depleted by as much as 80%. Quantitative X-ray fluorescence microscopy (XFM) reveals the same chemical trends in microchemical maps of stylolites in the Gudman Oolite[25], most easily visualised as Fe enrichment and Ca depletion (Fig. 2b).

In the following, we employ quantitative high-resolution XFM and X-ray ptychography, also known as scanning X-ray diffraction microscopy, to characterise densely packed micro-dissolution seams within the Kaiwhata limestones. Our results suggest that these micro-dissolution seams formed during shallow burial diagenesis and mobilised about 10% of the total carbon stored in the studied deep-sea limestones, similar to stylolites, their macroscopic counterparts. We hypothesise that the tectonic setting determines the fate of the liberated carbon. In deep-sea sediments residing in tectonically quiescent regions, dissolved carbon is probably reprecipitated as cement, driving lithification and sealing of the carbonate mud. In contrast, in tectonically active regions, advective driving forces can return the freed carbon back into the ocean. In conclusion, micro-dissolution is predicted to play an important role during carbon exchange and redistribution in Earth's largest carbon sink.

Results

Macroscopic dissolution structures. The Kaiwhata limestones contain burial-related diagenetic stylolites with length scales of tens of metres down to millimetres (Fig. 1). The largest, most pervasive stylolite family features wave-like stylolites at carbonate bedding interfaces, especially at contacts with siliciclastic interbeds, with a lateral extent of as much as 50 m (Fig. 1a). Their amplitudes are generally <3 cm and <25% of the bedding thickness. Diagenetic stylolites contained within limestone beds have lengths from a few centimetres to ca. 2 m, most commonly on the order of a few centimetres (Fig. 1b). They typically have residue thicknesses <1 mm with peak amplitudes between 100 and 500 µm and maxima to 5 mm. Layer-internal stylolites occur in wackestone beds with visible concentrations of detrital material (Fig. 1b) whereas calci-mudstones do not show macroscopically visible stylolites. Therefore, the dark fine-grained stylolite residue probably consists of insoluble detrital minerals accumulated passively within the dissolution plane. Some layer-internal stylolites are filled with the mm- to cm-thick residue of silty and sandy sediment (Fig. 1b), attesting to the low solubility of the siliciclastic detritus relative to the micrite and substantial bedding-perpendicular chemical compaction. Using the maximum amplitudes of bedding-interface stylolites alone, it is estimated that at least ~20% of the Kaiwhata limestone was dissolved by these structures.

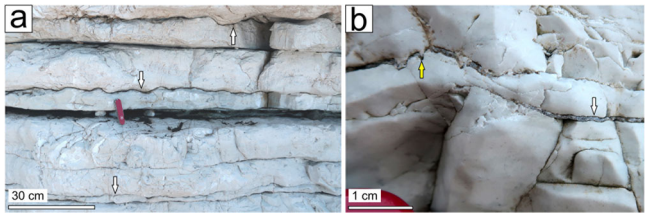

Fig. 1 Examples of macroscopic dissolution structures in outcrop. a Outcrop of the Kaiwhata limestones with flat-lying beds. White arrows mark large bedding-parallel diagenetic wave-like stylolites. **b** Close-up cross-sectional view of a horizontal wackestone bed. Dark-grey speckles are detrital grains. The yellow and white arrows mark bedding-internal diagenetic stylolites filled with siltstone. The yellow arrow marks a tell-tale stylolite "tooth".

Cryptic micro-scale dissolution structures. High-resolution XFM maps reveal diagenetic dissolution structures on the micro-scale in parts of the limestone free of macroscopically visible stylolites. Wackestone Sample A contains wavy zones parallel or at low angles to bedding (Fig. 3a), marked by strong Ca depletion and Fe enrichment (Fig. 3b, c) like the stylolites in the Gudman Oolite (Fig. 2b). These wavy structures have widths between 6 and 45 µm, lengths between 50 µm and 2 mm, a spacing between 5 and 325 µm, and locally wrap around less soluble, monomineralic, calcitic micro-fossils[26], forming anastomosing patterns (Fig. 3a). The Sr map of Sample A shows that these structures truncate the shells of otherwise barely deformed micro-fossils, a clear indication of calcite dissolution (Fig. 3d). Other tell-tale signs of calcite dissolution include the accumulation of insoluble Fe-rich platy minerals within the dissolution structures

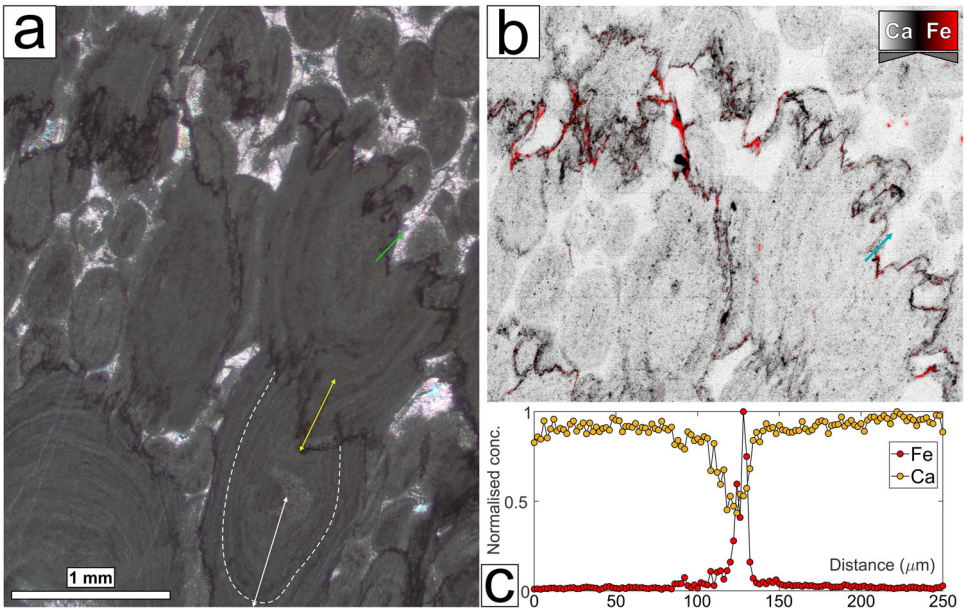

Fig. 2 Typical stylolites. a Transmitted-light micrograph with crossed polarisers of an oolitic grainstone of the Gudman Oolite[25]. The serrated, black zones are stylolites, which clearly dissolved the deformed, ellipsoidal ooids (dark-grey grains). This image demonstrates that stylolite tooth amplitude presents a lower-bound estimate to dissolution. The dashed white line traces a concentric primary growth layer of a dissolved ooid. The white arrow denotes the ooid long axis, which extends beyond the lower image margin. The stylolite at the upper tip of the ooid exhibits a maximum amplitude (yellow arrow) that is considerably smaller than the portion of the upper long axis that has been removed by dissolution. This effect is even more pronounced in the larger ooid above the discussed stylolite interface. The green arrow marks the location for the concentration profile shown in (**c**). **b** Micro-scale XFM map of the elements Ca (grey scale) and Fe (red scale) of the upper part of the micrograph seen in (**a**). Saturated colours indicate high element concentrations. Strongly serrated stylolites are characterised by low Ca concentrations (black colours) and high Fe concentrations (bright red colours). The blue arrow marks the position of the concentration profile in (**c**) and is 250 μm long. **c** An elemental cross-section across a stylolite shows that Ca is depleted by ~55% while Fe is enriched about 30 times within this stylolite. Here and in all following normalised elemental profiles, error bars are smaller than symbol size and thus not shown.

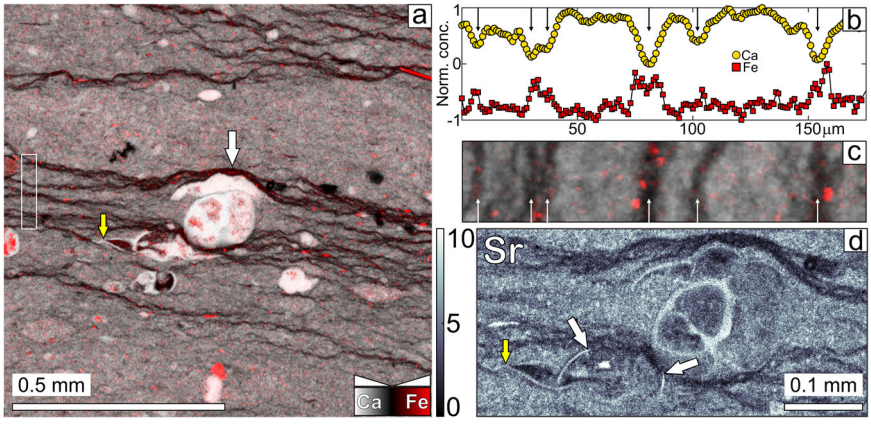

Fig. 3 Micro-dissolution seams in Sample A. a XFM map of the Kaiwhata limestone displaying Ca (grey scale) and Fe (red scale). Bedding is horizontal. The white arrow points to a dissolution structure with a thickness of 20 μm arrested by the micro-fossil underneath it. Fossils appear as bright white ellipsoidal objects. The white rectangle marks a zone for which normalised averaged elemental profiles are plotted in (**b**). **b** Averaged and normalised profiles of Ca and Fe traverse six dissolution structures with Ca depletion and Fe enrichment (black arrows). The Fe profile is shifted down by −1 for visibility. **c** Magnified view of the zone for which averaged elemental profiles in (**b**) were obtained. The white arrows mirror the black ones in (**b**). The map scale is given in (**b**). **d** This magnified view of the Sr map of Sample A demonstrates that the dissolution structures are also zones of Sr depletion and truncate fossil shells (white arrows). This map has a horizontal extent of 0.5 mm, and the yellow arrow serves as location reference to the larger map in (**a**). The concentration unit is μg cm^{-2}. The XFM maps used to make this figure are provided in Supplementary Data 1.

and the occurrence of pressure shadows around micro-fossils[27], as discussed in detail further below.

Simultaneous micro-scale XFM and nano-scale X-ray ptychography of wackestone Sample B highlight more subtle dissolution structures (Figs. 4 and 5). XFM concentration maps of the elements Ca and Fe reveal slightly wavy, linear zones sub-parallel or at low angles to bedding (Fig. 4a). These zones have widths of ca. 10 μm, lengths to 500 μm, mean spacing of 42 μm (Fig. 4), and share the same chemical signature of Fe enrichment and Ca depletion (Fig. 4b) as the dissolution structures in Sample A (Fig. 3), previously observed in stylolites[24], illustrated here with the Gudman Oolite[25] (Fig. 2b). Their morphology is also similar

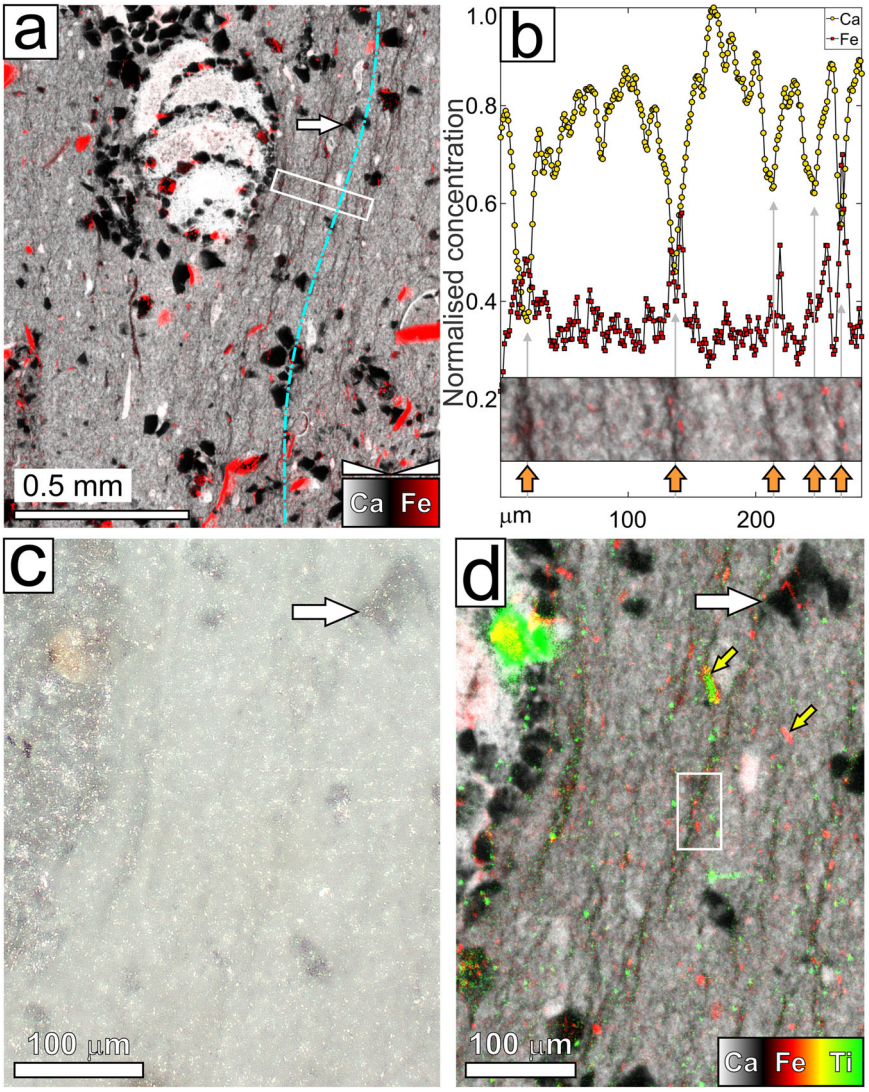

Fig. 4 Micro-dissolution seams in Sample B. a XFM map for a macroscopically stylolite-free wackestone sample of the Kaiwhata limestone displaying Ca (grey scale) and Fe (red scale). Sedimentary bedding is vertical. On the right side of the large fossil in the central top of the image, an array of micro-dissolution seams is visible, similarly marked by Ca depletion and Fe enrichment. The blue dash-dot line shows the averaged seam orientation wrapping around and merging with the bedding orientation below the micro-fossil. The white rectangle marks an area, for which averaged Ca and Fe concentrations profiles normal to the dissolution seams have been obtained, shown in (**b**). The Fe profile in **b** is shifted downwards by 0.3 units for legibility. Ca is depleted by ca. 40% while Fe is enriched by about 67% in the seams. The inset shows a magnified view of the white box in (**a**) where arrows mark the positions of micro-dissolutions seams. Fe-rich phases have elongated ellipsoidal or rectangular shapes aligned with bedding. **c** Reflected-light micrograph of the studied wackestone sample. The white arrow serves as spatial reference to the corresponding three-element XFM map in (**d**). Dissolution seams appear as very faint schlieren in (**c**) but are clearly visible in the micro-chemical map (**d**). Grey colours mark Ca concentrations, red colours correspond to Fe concentrations, and green colours denote Ti concentrations. Ca is depleted in seams (dark-grey colours) while Fe and Ti are enriched. The white rectangle marks an area containing a prominent micro-dissolution seam, for which XFM maps and nano-scale ptychography have been acquired (Fig. 5). The yellow arrows in (**d**) mark two prominent platy Ti- and Fe-rich minerals, which are not visible at the sample surface in (**c**). This observation highlights the important volumetric sampling capacity of XFM. The XFM maps used to make this figure are provided in Supplementary Data 2 and 3.

to the structures in Sample A and consistent with nascent micro-stylolites observed in low-strain regions of foliated carbonate fault rocks[28]. Therefore, we interpret the wavy zones of Ca-depletion and Fe-enrichment in both samples as micro-dissolution structures and adopt the term "micro-dissolution seam" to highlight the morphological difference to the more serrated stylolites[20] (Figs. 1 and 2). These micro-dissolution seams are not visible in hand specimens and do not form a penetrative cleavage or secondary foliation as do most rocks targeted for the study of dissolution seams[28–30]. Under the reflected-light microscope, the micro-dissolution seams appear as faint schlieren with a slightly darker grey colour than the matrix (Fig. 4c). Hence, similar structures may have been overlooked previously in deep-sea limestones.

In addition to Fe-rich minerals (Figs. 3a, 4a, 5b, h), Ti-bearing phases also are enriched in the micro-dissolution seams (Figs. 4d, 5c), consistent with bulk-chemical analyses of stylolite residue[24]. About 80% of both phases have strongly anisotropic rectangular or ellipsoidal shapes with aspect ratios between 1.5 and 5 (Figs. 3a, 4b, d, 5b, c). Therefore, most Fe phases are likely insoluble clay minerals, such as smectite and illite, rather than secondary oxides and hydroxides, which have isometric shapes[28]. Moreover, the Eocene mudstones conformably capping the Kaiwhata limestones are smectite-rich (≥85%)[13]. Some Ti-rich

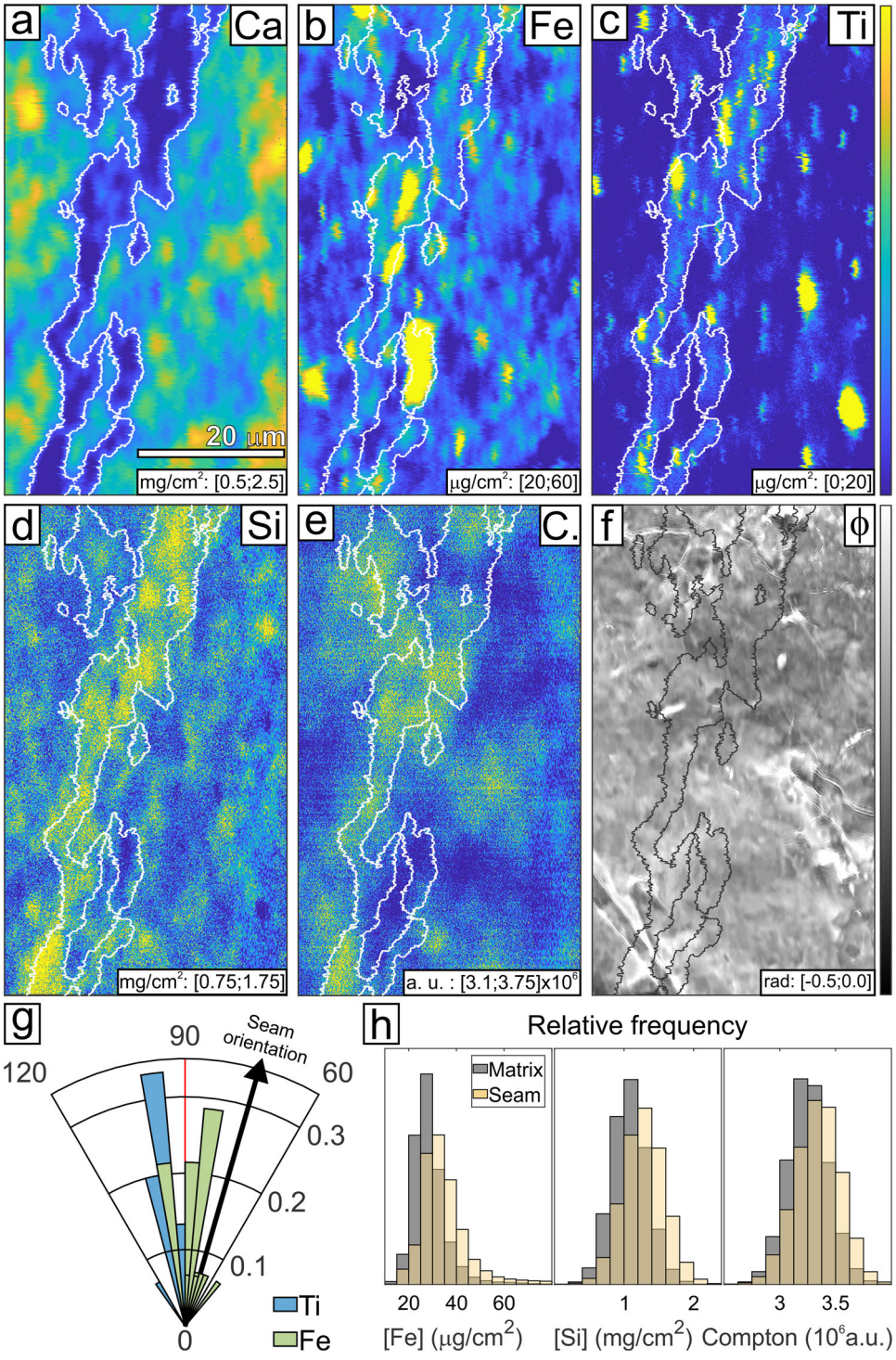

Fig. 5 Nano-scale chemical and structural maps of an individual micro-dissolution seam. a XFM Ca map of a micro-dissolution seam from Sample B and its immediate surroundings. Seam boundaries obtained with automated segmentation (see the "Methods" section) are marked with white lines. The maps in (**b**)–(**f**) have the same scale. **b** Fe map, **c** Ti map, **d** Si map, and **e** Compton scattering map for the same area shown in (**a**). Fe, Ti, and Si are enriched within the seam. The XFM map of Compton scattering intensity (arbitrary units) demonstrates higher intensity within seams, indicating a density increase. **f** Nano-scale ptychographic map of the phase (in radians) of the complex X-ray wavefield exiting the sample. The micro-dissolution seam does not display a marked structural difference in comparison to the micritic matrix. **g** Polar plot of the relative long-axis orientation-frequency distribution of Fe- and Ti-rich phases mapped in (**b**) and (**c**). Long-axis orientation was determined from best-fit ellipses to Fe particles with concentrations ≥50 µg/cm^2 and Ti particles with concentrations ≥of 15 µg/cm^2. To minimise discretization errors, phases made of <30 pixel and with aspect ratios <2 were disregarded. Most phases are aligned with bedding (vertical red line) within ±5°. **h** Histograms of the relative concentration frequency distributions of Fe and Si as well as Compton-scattering intensity, respectively, demonstrate that dissolution seams exhibit elevated magnitude of these quantities. The XFM maps and ptychogram used to make this figure are provided in Supplementary Data 4.

phases may be euhedral rutile (TiO_2), which is a common insoluble accessory mineral and has been observed in stylolite residue[28]. Another common accessory Ti phase with anisotropic shape is titanite ($CaTiSiO_5$), and some Ti-rich grains in the seam have Si enrichment (Fig. 5c, d). Si enrichment is a general feature of our micro-dissolution seams (Fig. 5d), as seen previously in cleavage seams[30]. In addition to minor titanite, phyllosilicates are the most likely host minerals. This interpretation is supported by the platy shape of most Fe-rich phases and the fact that regions with the highest Si concentrations also exhibit high aspect ratios with long axes sub-parallel to bedding (Figs. 3a, 5b, d). Moreover, sheet silicates are very common in stylolite residue[16,28]. On average, micro-dissolution seams also exhibit a higher intensity of Compton scattering than the micritic matrix (Fig. 5e, h), with a median increase relative to the matrix of 1.5% for all studied seams. As Compton scattering intensity is proportional to electron density and thus a proxy for mass density[31], we infer that the dissolution seams are denser than the micritic matrix, consistent with a passive enrichment of phyllosilicates.

In addition to the reported chemical and morphological evidence, the spatial configuration of the micro-dissolution seams and platy Fe- and Ti-rich phases within and around them confirm that they formed diagenetically (Figs. 3a, 4a, d, 5g). Both samples contain micro-fossils (Figs. 3a, 4a), which were more resistant to dissolution, likely because they consist of coarse, dense, mono-mineralic calcite[26]. Such fossils act like rigid objects during diagenetic compaction[20]. All XFM maps display micro-dissolution seams that wrap around prominent micro-fossils and merge with the bedding orientation away from the lateral tips of these rigid clasts (Figs. 3a, 4a). The approximately triangular areas immediately adjacent to the tips of the micro-fossils, however, do not contain micro-dissolution seams, consistent with the presence of a pressure shadow[27]. Similar pressure shadows and seam geometries were observed by Gratier et al. [27] in indenter-driven dissolution experiments on gypsum plaster were initially randomly distributed insoluble illite accumulated passively in 5–10 µm-thick micro-dissolution seams wrapping around the indenter. Moreover, Sample B shows that even where micro-dissolution seams are oblique to bedding (~17°) because of their vicinity to rigid micro-fossils, the long axes of anisotropic Fe- and Ti-rich grains are aligned with sedimentary bedding (±5°, Fig. 5b, c, g). The associated compaction strains, as shown below, are not large enough to cause the realignment of platy minerals with the seam due to passive rotation. Hence, the Fe- and Ti-rich grains must have obtained their shape-preferred orientation during deposition and before seam formation. A post-diagenetic origin of bedding-parallel dissolution structures can be ruled out by the consistent overprint by younger tectonic structures (Supplementary Fig. 2).

A nano-scale ptychogram is a high-resolution projected X-ray phase-contrast image of the sample[32,33] and thus well suited for visualising nano-scale voids and interfaces[34]. The ptychogram of Sample B reveals that the nano- and micro-structure of the micro-dissolution seam do not differ substantially from those of the micritic matrix (Fig. 5f). Therefore, pressure dissolution in this seam is mainly a chemical process without major reconfiguration of pores to the limit of resolution (~100 nm). In addition to their micrometric size and spacing, this observation explains why micro-dissolution seams have remained undetected. Moreover, as quantified below, micro-dissolution seams accommodate small volumetric strains and thus do not concentrate enough insoluble minerals to become macroscopically visible as opposed to mature stylolites. In contrast to reflected-light microscopy and other surface-imaging microscopic techniques such as scanning electron microscopy, XFM images Fe- and Ti-rich phases as well as Ca depletion non-destructively from sample depths to 30 µm (Fig. 4d; Supplementary Note 2, Supplementary Table 1)[35], thus allowing quantitative analysis of small concentration changes within the sample rather than just at the surface. This instrumental capability is key to the detection of the micro-dissolution seams.

Mass-balance calculations. High-resolution quantitative XFM maps also provide estimates of relative total mass loss, relative calcite loss, volumetric strain, and relative density changes within the cryptic micro-dissolution seams via a classic mass balance approach[21,22]. This approach requires the identification of insoluble elements to determine the mass factor (see the "Methods" section, Eqs. (1), (2), Supplementary Fig. 3). Previous chemical and microstructural analyses demonstrate that Fe, Si, and Zr can be considered insoluble in limestone-hosted stylolites and pressure dissolution seams[24,28,30]. In Sample A, only Fe and Zr concentrations are employed to measure the mass factor. Si is omitted because the sample was mounted on a high-purity quartz slide while being scanned at 18.5 keV. At this energy, the quartz slide adds to the fluorescence Si signal. In Sample B, we use the concentrations of Fe and Si to determine the mass factor. This sample was scanned free-standing at 10.1 keV, ideal conditions for X-ray ptychography at the XFM beamline[33]. With this setup, Si can be measured without bias of the sample mount, but the energy is too low to capture Zr. 69% of the regions examined in the mass-balance analysis of Sample B (Supplementary Fig. 4) display Fe and Si concentration ratios in the seam and matrix within ±10% of each other, supporting the notion that these elements are immobile in our samples. This assumption is also consistent with the shallow pressure and temperature trajectory of the studied rocks (Supplementary Note 1). Further, both elements are common within the micritic matrix, hosted in fine-grained minerals and micro-fossils such as radiolarians that exhibit an approximately uniform spatial distribution (Figs. 4d, 5b, c), rendering them excellent insoluble tracers for mass-balance analysis.

The mass-balance analysis for Sample A (see the "Methods" section) yields the following results. The median total mass loss in the seams is 13%, the associated median relative Ca loss is 51%, and the median volume loss in seams is 14%. In 2D, seams cover 18% of the area of the sample. Therefore, a median loss of Ca of 9.3% is obtained for the entire sample. Sample B contains a larger proportion of detrital clastic grains and fossils than Sample A, which could not be excluded easily from the mass-balance analysis with unsupervised segmentation. Therefore, we resorted to investigating 37 carefully chosen regions of interest-free from detrital material and fossils (see the "Methods" section, Supplementary Fig. 4). For mass-balance estimates of these rectangular regions of interest in Sample B (Fig. 6a, b), we found a median relative total mass loss per seam of 11% (mean: 12%, standard deviation STD: 8%), a median relative Ca loss per seam of 44% (mean: 45%, STD: 8%), and a median volume loss of 13% per seam (mean: 14%, STD: 9%). To determine the relative Ca loss, and hence relative carbon loss, for the whole sample, we adopted a one-dimensional scan-line approach (see the "Methods" section, Supplementary Figs. 4 and 5). For 15 equidistant scan lines perpendicular to bedding, and thus parallel to the uniaxial compaction direction, we measured the number of intercepted dissolution seams, their individual widths, and the total scan-line length occupied by seams (Fig. 6c, d). The number of dissolution seams ranges from 35 to 85, with a median of 61 (mean: 63, STD: 13), over a scan-line length of 2551 µm (Fig. 6c), giving a median spacing of 42 µm (mean: 42 µm, STD: 10 µm). The median width of individual seams is 5 µm (Fig. 6d, mean: 6 µm, STD: 5 µm). The total scan-line length occupied by seams spans the interval 216 to 485 µm with median 366 µm, which

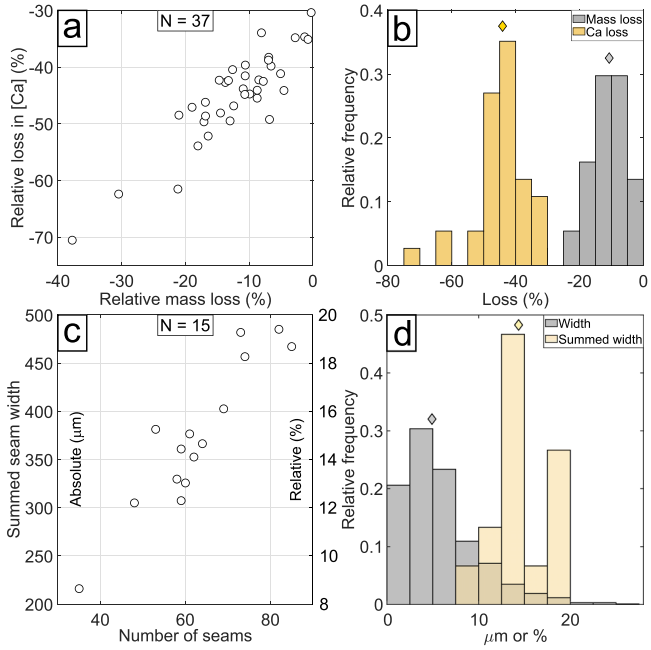

Fig. 6 Results of the mass-balance and scan-line analyses for Sample B. a Plot of the relative decrease in Ca concentration over relative total mass loss within micro-dissolution seams. **b** Histograms of the relative frequencies of the quantities plotted in (**a**). The diamonds above the histograms indicate the median. **c** Plot of total cumulative distance along a scan-line occupied by dissolution seams in absolute and relative values (compared to total scan-line length, right ordinate) over the total number of seams intercepted by a scan-line. **d** Relative frequency distribution of the absolute widths of individual dissolution seams (in µm, grey bars) and the relative cumulative width of dissolution seams along a scan-line (in %, yellow bars). The diamonds indicate the medians. The data used to make this figure are provided in Supplementary Data 4.

corresponds to a relative proportion between 8.5% and 19% (Fig. 6c) with a median of 14.4% (Fig. 6d). Since the sample contains ~15% siliciclastic grains that do not contribute to calcite dissolution and carbon loss (Supplementary Fig. 6), we reduce the effective scan-line length accordingly to 2168 µm. Using this number and the median cumulative seam length of 366 µm, ca. 17% of the dissolvable 1D calcite column is occupied by cryptic dissolution seams. Drawing on the median relative Ca loss per seam of 44%, we obtain an estimate of relative Ca loss of 7.4% for the whole sample. Considering only the carbon bound within calcite in rock samples A and B, the estimated relative carbon loss accommodated by micro-dissolution seams is equivalent to 9.3% and 7.4%, respectively, which is probably a conservative estimate (see the "Methods" section, Supplementary Fig. 5).

Discussion

These results suggest that the cryptic micro-dissolution seams can dissolve a substantial proportion of calcite, potentially mobilising large amounts of carbon and having a substantial influence on carbon storage in deep-sea limestones. Tectonically undeformed limestone cores from the stratigraphically equivalent[36] Amuri Formation were sampled offshore in New Zealand's Canterbury Basin in IODP Hole 317-U1352C and examined for diagenetic stylolites[37]. These core samples feature common bedding-parallel stylolites with spacings and amplitudes of about 1 cm, which dissolved between 7% and 12% of the Amuri Formation during diagenesis[37]. Therefore, the discovered micro-dissolution seams dissolve similar amounts of sediment as their mature macroscopic counterparts and should be considered in the long-term carbon budget of pelagic limestones. Hence, two important questions arise: at which burial depth and timescale do micro-dissolution seams form and where does the liberated carbon go?

Previous work documented the onset of stylolite formation in limestones at about 90 m burial depth and distributed macroscopic intergranular pressure solution at 30–40 m[38]. Since dissolution seams are precursors to fully developed stylolites[16,20,28], it is reasonable to predict that the micro-dissolution seams begin to form at shallower depths than the onset of macroscopic stylolites and intergranular pressure solution[38]. This view is compatible with a mathematical model for hydro-chemically driven stylolite formation considering clay-enhanced dissolution, diffusion, and precipitation[39]. This model predicts transport-limited stylolite growth and calcite dissolution rates from 1 mm to 1 m per million years, where the lower rates are characteristic of near-surface conditions[39]. For dissolution rates of 1 mm and 10 cm per million years as lower and upper bounds, it would take between 5000 and 50 years to grow a micro-dissolution seam of 5 µm width. Combining these temporal bounds with deep-sea burial rates between 1 and 10 cm per thousand years[40] gives a depth range for the onset of micro-dissolution seam formation between 0.5 mm and 50 cm. Since the surface mixed layer of deep-sea sediments is intensely reworked by burrowing organisms to an average depth of 10 cm[41], micro-dissolution seams probably cannot be preserved within it. The Kaiwhata limestones contain trace fossils such as *Zoophycos* and *Spirophyton* indicative of bioturbation, which are overprinted consistently by diagenetic stylolites. Micro-dissolution seams also would form below the depth of deepest bioturbation, but formation depths of decimetres to perhaps metres are consistent with the notion that the initiation of pressure dissolution in limestones does not require a minimum confining pressure and temperature[20].

Determining whether liberated carbon left the limestone package is more problematic. The reactive transport distance of the pore fluid carrying the dissolved carbon determines its destination. The transport distance depends on the relative magnitudes of the relevant fluid transport mechanisms, diffusion and advection[42]. The characteristic distance for diffusive porous transport of dissolved calcite prior to precipitation can be as low as 1–10 cm[39]. Therefore, a considerable proportion of the liberated carbonate may have been reprecipitated as pore cement while the sediment remained mechanically undisturbed[42]. However, mass-balance considerations for the stylolite-bearing pelagic limestones from IODP Hole 317-U1352C suggest that more than 50% of the dissolved calcite left the sedimentary system even though this offshore portion of the Amuri Formation remained tectonically undisturbed[37]. The physical key ingredient to lengthening the transport distance of the dissolved carbon, and thus to returning it to the overlying sediment or the hydrosphere, is fluid flow assisted by advection[42]. Potential physical mechanisms for adding an advective component to fluid flow include soft-sediment deformation[43], mechanical compaction[44], or the formation of synsedimentary fracture systems[45]. The studied limestones and their cover sediments feature clear evidence for advective drivers of pore-fluid flow discussed in the following. In fine-grained limestones, mechanical compaction is the dominant mechanism for pervasive porosity loss and associated fluid expulsion over the first 100 m of burial[44]. The Kaiwhata limestones contain interbedded siliciclastic turbidites, which include up to ~3 m-thick massive turbiditic sandstone beds that attest to intermittent periods of rapid sedimentation. Such fast sedimentation events must have been accompanied by accelerated mechanical compaction of the underlying limestones, providing an advective driver for pore-fluid expulsion. Moreover, the Kaiwhata limestones contain decimetre-wide bedding-perpendicular sandstone dikes, which commonly transect the entire sequence as

they emerge from thick sandstone beds near its base. These sandstone dikes formed when the sediment package was still poorly consolidated and are a common regional feature of the Kaiwatha Formation[46] and its regional equivalent, the Amuri limestone[36]. These structures may have scavenged free pore fluids from the host rocks and transported them into overlying strata or even back into the ocean. The sandstone dikes, and all silt- and sandstones intercalated in the Kaiwhata limestones, contain calcite cement, attesting to mobile, carbonate-saturated pore fluids. In addition, sedimentary stylolites, the mature equivalent of the described micro-dissolution seams, can form large-scale interconnected 3D networks with cogenetic high-angle extension fractures, represented by veins and joints, which may act as fast vertical drainage pathways[45]. In the studied rocks, bedding-perpendicular veins generally postdate micro-dissolution seams (Supplementary Fig. 2). Therefore, veins probably did not contribute to removing carbon dissolved by the seams in our research area. Bedding-perpendicular diagenetic joints, i.e., uncemented extension fractures, were also not observed. However, such early joints would have poor preservation potential, considering the later tectonic history of the Kaiwhata Formation. Mechanically, it is conceivable that cogenetic transient joints formed during micro-dissolution when the fluid channelled along the seams attained sufficiently high pore-fluid pressure to induce brittle failure at the tips or flanks of the seams[47]. Finally, the onset of subduction in the research area coincided with widespread deposition of olistostromes in the Eocene and Miocene strata overlying the Kaiwhata limestone[13,48]. These thick debris-flow deposits entrained portions of the poorly consolidated limestone[13] and would have imposed mechanical disturbance on their substratum associated with the liberation of free pore fluids. Other indicators of tectonically induced synsedimentary fluid flow such as structurally controlled cold seeps through tubular carbonate concretions[49] and millimetre- to metre-scale convoluted bedding in turbidites[50] are very common and regionally widespread throughout the Miocene strata overlying the Kaiwhata Formation. Hence, there is no doubt that pore fluids were highly mobile in the shallowly buried sediments of the Miocene Hikurangi subduction wedge.

Therefore, we propose that the fate of carbon liberated by cryptic micro-dissolution largely depends on the tectonic lifecycle of deep-sea limestones. Far away from subduction boundaries, the carbonate sediment remains largely undisturbed and poorly consolidated, and most of the dissolved carbon probably reprecipitates in limestone micro-pores, driving lithification. If micro-dissolution occludes 10% of the primary porosity, sediment permeability can drop by a factor of 10[51]. In this scenario, micro-dissolution would improve carbon retention in pelagic limestones by improving their sealing capacity and reducing their solubility[26]. However, when deep-sea limestones reach the subduction boundary, increasingly rapid sedimentation, seismicity, and the onset of tectonic sediment deformation provide advective drivers for fluid expulsion, which can return the liberated carbon into overlying strata or the ocean. Regardless of whether or not the dissolved carbon remains within the system or is returned to the ocean, the discovered micro-mechanism for calcite mobilisation is predicted to have a substantial impact on fluid and gas flux at the interface between the hydrosphere and geosphere in the deep sea on time scales of tens to thousands of years. In conclusion, we advocate that core samples of limestones in different tectonic settings recovered from deep-sea drilling should be examined systematically with spatially resolved micro- and nano-chemical and -structural mapping. Analysis of such samples will enable rigorous tests of our predictions, overcome the limitations of small sample size from one geographic location, and ultimately provide improved estimates for the abundance of micro-dissolution seams, their formation depth, and the fate of the dissolved carbon.

Methods

XFM and ptychography

Sample A. Rock slices were embedded in epoxy and mounted on 1 mm-thick quartz-glass slides before polishing to <30 µm thickness. Sections were mounted with standard sample mounts for analysis at the XFM beamline of the Australian Synchrotron[52]. A square area of 1 mm^2 was scanned continuously at a velocity of 0.5 mm s^{-1} with a sampling interval of 1 µm in both the vertical and horizontal directions through an 18.5 keV X-ray beam focused to a ~2 µm spot at the sample using a Kirkpatrick–Baez mirror pair, yielding a resolution of ~1.5 µm with an effective pixel dwell time of 2 ms. Excited X-ray fluorescence was collected in event mode using a Maia (Rev D) detector system[53,54] positioned in its typical backscatter geometry (Supplementary Fig. 8). Spectra were deconvoluted using the dynamic analysis[55] method implemented in GeoPIXE[56] and quantified using known metallic foils, producing quantitative images of elements from sulphur to zirconium inclusive. All XFM maps for Sample A are provided in Supplementary Data 1 as uncompressed 32-bit tiffs.

Sample B. Rocks were prepared for analysis by thin sectioning to <30 µm thickness without resin embedding. Thin sections were presented to the beam at the XFM beamline at the Australian Synchrotron[52] leaving the region of interest free-standing to allow the transmitted beam to pass through. A large area elemental map (2.5 mm × 1.8 mm) was collected by scanning the section continuously at a velocity of 2 mm s^{-1} with a sampling interval of 1 µm in both the horizontal and vertical direction through a 10.1 keV X-ray beam focused to a ~1 µm spot at the sample using a Kirkpatrick–Baez mirror pair, yielding a resolution of ~1 µm with an effective per-pixel dwell of 0.5 ms. Fluorescent photons were collected and analysed as described above, obtaining quantitative XFM maps of elements from sulfur to zinc inclusive.

From this elemental map a smaller region of interest (60 µm × 80 µm) was selected for interrogation with simultaneous X-ray fluorescence and ptychography to obtain the projected structural and chemical information. Using the same 10.1 keV focus described above, the section was scanned continuously in the horizontal direction at 5 µm s^{-1} with a sampling interval in the horizontal and vertical directions of 100 nm, yielding an effective dwell of 20 ms per pixel. X-ray fluorescence data were collected and analysed as described previously. Diffraction data were collected in the far-field using a Dectris Eiger2 X 1M pixelated X-ray detector placed ~3.67 m downstream of the focus using a triggering system described by Jones et al. [33] (Supplementary Fig. 8). The set of 427,718 diffraction patterns was cropped to 128 × 128 pixels and distributed onto three nodes of the high-performance computing system at QUT and reconstructed using a GPU implementation of the ePIE reconstruction algorithm[57,58] before being recombined in Fourier space to obtain a single image[59]. The resulting reconstructed pixel size is ~47 nm. All XFM maps and the ptychogram for Sample B are provided in Supplementary Data 2–4 as uncompressed 32-bit tiffs.

Mass balance estimates. We use the Isocon method[21,22,60] to estimate dissolution-related mass fluxes and concentration changes in our sample. The mass balance of phase i in a metasomatically altered rock can be written as[60]

$$C_i^{\mathrm{A}} = \frac{m^{\mathrm{H}}}{m^{\mathrm{A}}}\left(C_i^{\mathrm{H}} + \triangle C_i\right). \quad (1)$$

C_i denotes the concentration of phase i, superscript H indicates the unaltered host rock (the micritic matrix surrounding the seams, Supplementary Fig. 3), superscript A designates the altered rock (the rock within dissolution seams, Supplementary Fig. 3), m is mass, and $\triangle C_i = \frac{\triangle m_i}{m^{\mathrm{H}}} = \frac{m_i^{\mathrm{A}} - m_i^{\mathrm{H}}}{m^{\mathrm{H}}}$ is the dimensionless relative mass gain of phase i relative to the reference total mass of the host rock m^{H}. The ratio $M = \frac{m^{\mathrm{H}}}{m^{\mathrm{A}}}$ is the inverse of the enrichment factor, also called the mass factor. M can be determined if immobile phases can be identified. We assume that in our sample Fe and Si are immobile ($\triangle C_{\mathrm{Fe}} = \triangle C_{\mathrm{Si}} = 0$) and that both phases are, to first order, distributed homogeneously in the host rock. In this case, Eq. (1) simplifies to

$$C_i^{\mathrm{A}} = MC_i^{\mathrm{H}}. \quad (2)$$

A non-linear least-squares fit Eq. (2) using two data points for Fe and Si is employed to determine M (Supplementary Fig. 3c). The procedure for extracting Fe and Si concentrations for unaltered matrix and altered dissolution seams is described further below. Once M is known, one can compute the relative concentration change of the mobile phases of interest, in our case Ca, by substituting M into Eq. (1) and rearranging:

$$\frac{C_{\mathrm{Ca}}^{\mathrm{A}}}{M} - C_{\mathrm{Ca}}^{\mathrm{H}} = \triangle C_{\mathrm{Ca}} \Longleftrightarrow \frac{C_{\mathrm{Ca}}^{\mathrm{A}}}{C_{\mathrm{Ca}}^{\mathrm{H}}}\frac{1}{M} - 1 = \frac{\triangle C_{\mathrm{Ca}}}{C_{\mathrm{Ca}}^{\mathrm{H}}}. \quad (3)$$

Since Ca is lost due to the decomposition of $CaCO_3$, the relative concentration change of C is directly proportional to that of Ca. Relative total mass loss in

micro-dissolution seams (Fig. 6a, b) is given by

$$\frac{m^{\mathrm{A}} - m^{\mathrm{H}}}{m^{\mathrm{H}}} = \frac{m^{\mathrm{A}}}{m^{\mathrm{H}}} - 1 = \frac{1}{M} - 1. \quad (4)$$

When the density ratio of host and altered rock can be determined, the volume change can be computed:

$$\frac{m^{\mathrm{H}}}{m^{\mathrm{A}}} = M = \frac{\rho^{\mathrm{H}} V^{\mathrm{H}}}{\rho^{\mathrm{A}} V^{\mathrm{A}}} \Longleftrightarrow \frac{V^{\mathrm{A}}}{V^{\mathrm{H}}} = \frac{\rho^{\mathrm{H}}}{M\rho^{\mathrm{A}}}, \quad (5)$$

where ρ denotes density.

In Sample B, we computed relative Ca loss (Eq. (3)) and relative total mass loss (Eq. (4)) for 37 rectangular regions of interest (ROI) in our XFM maps (Supplementary Fig. 4). We chose ROIs that exclusively contain micritic matrix and dissolution seams but are free of siliciclastic detrital grains, calcite veins and insoluble fossils. In each ROI, unaltered host rock—the micritic matrix—was segmented from altered dissolution seams by binary thresholding of Ca maps (Supplementary Fig. 3a, b). Pixels with C_{Ca} greater than the difference between the global median C_{Ca} and the global standard deviation of C_{Ca} in a given ROI were classified as matrix while the remaining ones were designated as micro-dissolution seams (Supplementary Fig. 3b). In a second segmentation step, we discarded isolated pixel clusters labelled as seams consisting of <50 pixels. After segmentation, the concentrations of Ca, Fe, and Si were extracted for matrix and seams in each ROI. The medians of the concentration frequency distributions (Supplementary Fig. 3d, e) were then employed for Isocon analysis in each ROI (Supplementary Fig. 3c). Since Sample A contains only a few fossils and detrital grains, these could be removed easily from the relevant element maps through binary thresholding of the Ca and Fe maps. The cleaned-up maps were treated with the same procedure as the individual ROIs in Sample B outlined above.

Spatial statistics of micro-dissolution seams. For spatial statistics of the widths and frequency of micro-dissolution seams in Sample B (Fig. 6c, d), a scan-line approach was used. 15 scan lines perpendicular to bedding, and hence micro-dissolution seams, with a constant spacing of 100 µm were examined in the Ca map (Supplementary Fig. 4). Sections where scan lines intercepted clastic grains, veins or fossils were excluded, as in the Isocon analysis. Along each scan-line, individual micro-dissolution seams were designated as troughs (negative peaks) in the Ca profile with a minimum trough depth equal to the difference between the global median C_{Ca} and the global standard deviation of C_{Ca}, as in the segmentation approach for the Isocon analysis. To avoid erroneous seam counts due to high-frequency noise, a minimum seam distance of 8 µm was enforced. The width of individual seams was measured at half prominence. This method is resistant to noise-related sampling artefacts but probably underestimates seam width systematically (Supplementary Fig. 5). Therefore, our seam-width statistics constitute a lower-bound estimate (Fig. 6c, d).

Data availability

The data used to produce the results of this article are available for download in Supplementary Data 1–4. The data can also be accessed at the Open Science Framework: https://doi.org/10.17605/OSF.IO/NT7K5

Received: 2 November 2020; Accepted: 12 August 2021;
Published online: 27 August 2021

References

1. Müller, R. D. & Dutkiewicz, A. Oceanic crustal carbon cycle drives 26-million-year atmospheric carbon dioxide periodicities. *Sci. Adv.* **4**, eaaq0500 (2018).
2. Kelemen, P. B. & Manning, C. E. Reevaluating carbon fluxes in subduction zones, what goes down, mostly comes up. *Proc. Natl Acad. Sci. USA* **112**, E3997 (2015).
3. Matter, J. M. & Kelemen, P. B. Permanent storage of carbon dioxide in geological reservoirs by mineral carbonation. *Nat. Geosci.* **2**, 837–841 (2009).
4. Ague, J. J. & Nicolescu, S. Carbon dioxide released from subduction zones by fluid-mediated reactions. *Nat. Geosci.* **7**, 355–360 (2014).
5. Wong, K. et al. Deep carbon cycling over the past 200 million years: a review of fluxes in different tectonic settings. *Front. Earth Sci.* **7**, (2019) https://doi.org/10.3389/feart.2019.00263.
6. Clift, P. D. A revised budget for Cenozoic sedimentary carbon subduction. *Rev. Geophys.* **55**, 97–125 (2017).
7. Dutkiewicz, A., Müller, R. D., Cannon, J., Vaughan, S. & Zahirovic, S. Sequestration and subduction of deep-sea carbonate in the global ocean since the Early Cretaceous. *Geology* **47**, 91–94 (2018).
8. Ridgwell, A. & Zeebe, R. E. The role of the global carbonate cycle in the regulation and evolution of the Earth system. *Earth Planet. Sci. Lett.* **234**, 299–315 (2005).
9. Plank, T. In *Treatise on Geochemistry* 2nd edn (eds Holland, H. D. & Turekian, K. K.) 607–629 (Elsevier, 2014).
10. Morse, J. W. In *Treatise on Geochemistry* (eds Holland, H. D. & Turekian, K. K.) 67–85 (Pergamon, 2003).
11. Morse, J. W. & Arvidson, R. S. The dissolution kinetics of major sedimentary carbonate minerals. *Earth-Sci. Rev.* **58**, 51–84 (2002).
12. Van den Heuvel, H. B. The geology of the flat point area, eastern Wairarapa. *N. Z. J. Geol. Geophys.* **3**, 309–320 (1960).
13. Chanier, F. & Ferrière, J. From a passive to an active margin; tectonic and sedimentary processes linked to the birth of an accretionary prism (Hikurangi Margin, New Zealand). *Bull. Soc. Geol. Fr.* **162**, 649–660 (1991).
14. Chanier, F. & Ferrière, J. Extensional deformation across an active margin, relations with subsidence, uplift, and rotations: the Hikurangi subduction, New Zealand. *Tectonics* **18**, 862–876 (1999).
15. Park, W. C. & Schot, E. H. Stylolites; their nature and origin. *J. Sediment. Res.* **38**, 175–191 (1968).
16. Toussaint, R. et al. Stylolites: a review. *J. Struct. Geol.* **114**, 163–195 (2018).
17. Koehn, D., Renard, F., Toussaint, R. & Passchier, C. W. Growth of stylolite teeth patterns depending on normal stress and finite compaction. *Earth Planet. Sci. Lett.* **257**, 582–595 (2007).
18. Ebner, M., Koehn, D., Toussaint, R., Renard, F. & Schmittbuhl, J. Stress sensitivity of stylolite morphology. *Earth Planet. Sci. Lett.* **277**, 394–398 (2009).
19. Ebner, M., Toussaint, R., Schmittbuhl, J., Koehn, D. & Bons, P. Anisotropic scaling of tectonic stylolites: a fossilized signature of the stress field? *J. Geophys. Res.* **115**, (2010) https://doi.org/10.1029/2009JB006649.
20. Gratier, J.-P., Dysthe, D. K. & Renard, F. In *Advances in Geophysics* (ed. Dmowska, R.) Vol. 54, 47–179 (Elsevier, 2013).
21. Gresens, R. L. Composition–volume relationships of metasomatism. *Chem. Geol.* **2**, 47–65 (1967).
22. Grant, J. A. The isocon diagram; a simple solution to Gresens' equation for metasomatic alteration. *Econ. Geol.* **81**, 1976–1982 (1986).
23. Gratier, J. P. Estimation of volume changes by comparative chemical analyses in heterogeneously deformed rocks (folds with mass transfer). *J. Struct. Geol.* **5**, 329–339 (1983).
24. Renard, F., Schmittbuhl, J., Gratier, J.-P., Meakin, P. & Merino, E. Three-dimensional roughness of stylolites in limestones. *J. Geophys. Res.* **109**, (2004) https://doi.org/10.1029/2003JB002555.
25. Webb, G. E. Quantitative analysis and Paleoecology of earliest Mississippian Microbial Reefs, Gudman Formation, Queensland, Australia: not Just post-disaster phenomena. *J. Sediment. Res.* **75**, 877–896 (2005).
26. van den Ende, M. P. A., Niemeijer, A. R. & Spiers, C. J. Influence of grain boundary structural evolution on pressure solution creep rates. *J. Geophys. Res.* **124**, 10210–10230 (2019).
27. Gratier, J.-P., Noiriel, C. & Renard, F. Experimental evidence for rock layering development by pressure solution. *Geology* **43**, 871–874 (2015).
28. Viti, C., Collettini, C. & Tesei, T. Pressure solution seams in carbonatic fault rocks: mineralogy, micro/nanostructures and deformation mechanism. *Contrib. Mineral. Petrol.* **167**, 970 (2014).
29. Nenna, F. & Aydin, A. The formation and growth of pressure solution seams in clastic rocks: a field and analytical study. *J. Struct. Geol.* **33**, 633–643 (2011).
30. Gratier, J. P. et al. Geological control of the partitioning between seismic and aseismic sliding behaviours in active faults: evidence from the Western Alps, France. *Tectonophysics* **600**, 226–242 (2013).
31. Odeblad, E. & Norhagen, Å. Measurements of electron densities with the aid of the compton scattering process. *Acta Radiol.* **45**, 161–167 (1956).
32. Dierolf, M. et al. Ptychographic X-ray computed tomography at the nanoscale. *Nature* **467**, 436–439 (2010).
33. Jones, M. W. M. et al. Simultaneous X-ray fluorescence and scanning X-ray diffraction microscopy at the Australian synchrotron XFM beamline. *J. Synchrotron Radiat.* **23**, 1151–1157 (2016).
34. Ciani, A. et al. Ptychographic X-ray CT characterization of the osteocyte lacuno-canalicular network in a male rat's glucocorticoid induced osteoporosis model. *Bone Rep.* **9**, 122–131 (2018).
35. Henke, B. L., Gullikson, E. M. & Davis, J. C. X-ray interactions: photoabsorption, scattering, transmission, and reflection at $E = 50$–$30{,}000$ eV, $Z = 1$–92. *At. Nucl. Data Tables* **54**, 181–342 (1993).
36. Browne, G. H. In situ and intrusive sandstone in Amuri fades limestone at Te Kaukau Point, southeast Wairarapa, New Zealand. *N. Z. J. Geol. Geophys.* **30**, 363–374 (1987).
37. Vandeginste, V. & John, C. M. Diagenetic implications of stylolitization in Pelagic carbonates, Canterbury Basin, Offshore New Zealand. *J. Sediment. Res.* **83**, 226–240 (2013).
38. Tada, R. & Siever, R. Pressure solution during diagenesis. *Annu. Rev. Earth Planet. Sci.* **17**, 89–118 (1989).
39. Angheluta, L., Mathiesen, J. & Aharonov, E. Compaction of porous rock by dissolution on discrete stylolites: a one-dimensional model. *J. Geophys. Res.* **117**, (2012) https://doi.org/10.1029/2012JB009245.

40. Hüneke, H. & Henrich, R. In *Developments in Sedimentology* Vol. 63 (eds Hüneke, H. & Mulder, T.) Vol. 63, 215–351 (Elsevier, 2011).
41. Wetzel, A. & Uchman, A. In *Developments in Sedimentology*, (eds Knaust, D. & Bromley, R. G.) Vol. 64, 673–701 (Elsevier, 2012).
42. Fantle, M. S., Barnes, B. D. & Lau, K. V. The role of diagenesis in shaping the geochemistry of the marine carbonate record. *Annu. Rev. Earth Planet. Sci.* **48**, 549–583 (2020).
43. Alves, T. M. Submarine slide blocks and associated soft-sediment deformation in deep-water basins: a review. *Mar. Pet. Geol.* **67**, 262–285 (2015).
44. Croizé, D., Renard, F. & Gratier, J.-P. in *Advances in Geophysics*, Vol. 54 (ed. Dmowska, R.) 181–238 (Elsevier, 2013).
45. Laronne Ben-Itzhak, L., Aharonov, E., Karcz, Z., Kaduri, M. & Toussaint, R. Sedimentary stylolite networks and connectivity in limestone: large-scale field observations and implications for structure evolution. *J. Struct. Geol.* **63**, 106–123 (2014).
46. Eade, J. V. Stratigraphy and structure of the Mount Adams Area, Eastern Wairarapa. *Trans. R. Soc. N. Z.* **4**, 103–112 (1966).
47. Aharonov, E. & Karcz, Z. How stylolite tips crack rocks. *J. Struct. Geol.* **118**, 299–307 (2019).
48. Delteil, J., de Lepinay, B. M., Morgans, H. E. G. & Field, B. D. Olistostromes marking tectonic events, East Coast, New Zealand. *N. Z. J. Geol. Geophys.* **49**, 517–531 (2006).
49. Malie, P. et al. Spatial distribution and tectonic framework of fossil tubular concretions as onshore analogues of cold seep plumbing systems, North Island of New Zealand. *Bull. Soc. Géol. Fr.* **188** (2017) https://doi.org/10.1051/bsgf/2017192.
50. Field, B. D. Cyclicity in turbidites of the Miocene Whakataki Formation, Castlepoint, North Island, and implications for hydrocarbon reservoir modelling. *N. Z. J. Geol. Geophys.* **48**, 135–146 (2005).
51. Lucia, F. J. *Carbonate Reservoir Characterization—An Integrated Approach* 2nd edn (Springer-Verlag, 2007).
52. Paterson, D. et al. The X-ray fluorescence microscopy beamline at the Australian synchrotron. *AIP Conf. Proc.* **1365** (2011) https://doi.org/10.1063/1.3625343.
53. Siddons, D. P. et al. Maia X-ray microprobe detector array system. *J. Phys.* **499**, 012001 (2014).
54. Ryan, C. et al. The Maia detector and event mode. *Synchrotron Radiat. News* **31**, 21–27 (2018).
55. Ryan, C. G. & Jamieson, D. N. Dynamic analysis: on-line quantitative PIXE microanalysis and its use in overlap-resolved elemental mapping. *Nucl. Instrum. Methods Phys. Res. Sect. B* **77**, 203–214 (1993).
56. Ryan, C. G. et al. Nuclear microprobe—synchrotron synergy: towards integrated quantitative real-time elemental imaging using PIXE and SXRF. *Nucl. Instrum. Methods Phys. Res. B* **231**, 183–188 (2005).
57. Nashed, Y. S. G. et al. Parallel ptychographic reconstruction. *Opt. Express* **22**, 32082–32097 (2014).
58. Maiden, A. M. & Rodenburg, J. M. An improved ptychographical phase retrieval algorithm for diffractive imaging. *Ultramicroscopy* **109**, 1256–1262 (2009).
59. Jones, M. W. M. et al. Simultaneous nanostructure and chemical imaging of intact whole nematodes. *Chem. Commun.* **55**, 1052–1055 (2019).
60. Grant, J. A. Isocon analysis: a brief review of the method and applications. *Phys. Chem. Earth Parts A/B/C* **30**, 997–1004 (2005).

Acknowledgements

This research was undertaken on the XFM beamline at the Australian Synchrotron, part of ANSTO. The authors gratefully acknowledge funding by the Australian Research Council through Discovery grant DP170104550. We are deeply thankful to the Cameron family for access to their land and their warm hospitality at Pahaoa, New Zealand. Donald McAuley and Gus Luthje are thanked for sample preparation. We acknowledge the Central Analytical Facility of the Queensland University of Technology for their support with light and scanning-electron microscopy. Computational resources and services used in this work were provided by the eResearch Office of the Queensland University of Technology.

Author contributions

C.E.S. and M.M.W.J. designed the study. M.M.W.J., D.J.P., C.E.S., and L.D.N. performed the XFM experiment on Kaiwhata limestone. D.J.P. set up and calibrated this experiment and processed the raw data together with M.M.W.J. M.M.W.J., C.M.K., G.A.v.R., and C.E.S. conducted the XFM/ptychography experiment on the Kaiwhata limestone Sample B. C.M.K. set up and calibrated the beamline. M.W.M.J. and G.A.v.R. processed the raw data. K.E.E., C.E.S., C.R.S., L.D.N., and K.R.L. conducted the fieldwork at Pahaoa. G.E.W., L.D.N., D.J.P., and C.E.S. performed the XFM measurements on the Gudman Oolite. D.J.P. set up and calibrated this experiment and processed the raw data. G.E.W. provided the Gudman sample. C.E.S. conducted all quantitative analyses on the XFM maps and wrote the first draft of the manuscript. All authors contributed to further versions. K.R.-L. and C.E.S. obtained research funding for this study from the Australian Research Council.

Competing interests

The authors declare no competing interests.

Additional information

Supplementary information The online version contains supplementary material available at https://doi.org/10.1038/s43247-021-00257-w.

Correspondence and requests for materials should be addressed to C.E.S. or M.M.W.J.

Peer review information *Communications Earth & Environment* thanks Renaud Toussaint and the other, anonymous, reviewer(s) for their contribution to the peer review of this work. Peer reviewer reports are available. Primary handling editors: Mojtaba Fakhraee, Joe Aslin

Reprints and permission information is available at http://www.nature.com/reprints

Publisher's note Springer Nature remains neutral with regard to jurisdictional claims in published maps and institutional affiliations.